

Origins of sharp cosmic-ray electron structures and the DAMPE excess

Xian-Jun Huang^{a,b}, Yue-Liang Wu^a, Wei-Hong Zhang^a, and Yu-Feng Zhou^a

^a CAS Key Laboratory of Theoretical Physics, Institute of Theoretical Physics,
Chinese Academy of Sciences, Beijing, 100190, China,

University of Chinese Academy of Sciences, Beijing 100049, China, and

^b Sichuan University of Science and Engineering, Zigong 643000, China.

Nearby sources may contribute to cosmic-ray electron (CRE) structures at high energies. Recently, the first DAMPE results on the CRE flux hinted at a narrow excess at energy ~ 1.4 TeV. We show that in general a spectral structure with a narrow width appears in two scenarios: I) “*Spectrum broadening*” for the continuous sources with a δ -function-like injection spectrum. In this scenario, a finite width can develop after propagation through the Galaxy, which can reveal the distance of the source. Well-motivated sources include mini-spikes and subhalos formed by dark matter (DM) particles χ_s which annihilate directly into e^+e^- pairs. II) “*Phase-space shrinking*” for burst-like sources with a power-law-like injection spectrum. The spectrum after propagation can shrink at a cooling-related cutoff energy and form a sharp spectral peak. The peak can be more prominent due to the energy-dependent diffusion. In this scenario, the width of the excess constrains both the power index and the distance of the source. Possible such sources are pulsar wind nebulae (PWNe) and supernova remnants (SNRs). We analysis the DAMPE excess and find that the continuous DM sources should be fairly close within ~ 0.3 kpc, and the annihilation cross sections are close to the thermal value. For the burst-like source, the narrow width of the excess suggests that the injection spectrum must be hard with power index significantly less than two, the distance is within $\sim (3 - 4)$ kpc, and the age of the source is ~ 0.16 Myr. In both scenarios, large anisotropies in the CRE flux are predicted. We identify possible candidates of mini-spike and PWN sources in the current Fermi-LAT 3FGL and ATNF catalog, respectively. The diffuse γ -rays from these sources can be well below the Galactic diffuse γ -ray backgrounds and less constrained by the Fermi-LAT data, if they are located at the low Galactic latitude regions.

Introduction. Cosmic-ray (CR) electrons and positrons (CREs) with energies above TeV plays an important role in understanding the nearby origins of CRs within a few kpc [1]. Structures in the energy spectrum of CREs are expected, if the nearby sources are dominated by one or a few discrete sources. The current space experiments have begun to directly probe this energy region. For instance, the AMS-02 [2], Fermi-LAT [3] and CALET [4] experiments have measured the flux of CRE up to 1, 2 and 3 TeV, respectively, without observing any significant structures so far. Recently, the DAMPE experiment has reported the first high energy resolution measurement of the CRE flux up to 4.6 TeV [5]. The measured energy spectrum of CRE steepened above ~ 0.9 TeV, consistent with the results from the ground-based atmospheric Cherenkov telescopes [6–10]. Of interest, the DAMPE data also hinted at an excess over the expected background in a narrow energy interval $\sim (1.3 - 1.5)$ TeV. Making use of the DAMPE data in the energy range 55 GeV–4.6 TeV, and assuming a broken power-law background flux, we find that the local and global significance of the possible narrow excess is $\sim 3.7 \sigma$ and $\sim 2.5 \sigma$, respectively (details of the data analysis are shown in the supplementary material).

In light of the possible DAMPE “excess”, it is of general interest to address the question of what kind of sources are responsible for a sharp spectral feature in CRE flux. In this work, we explore the origins of a sharp spectral structure and emphasize that the space-time lo-

cation of source can be inferred from the spectral feature of the CRE flux. We show that in general a sharp spectral structure can be produced in two complementary scenarios: I) for continuous sources with a line-shape injection spectrum, a finite width can develop after propagation in the Galaxy (dubbed “spectrum broadening”). Well-motivated sources are nearby DM substructures such as mini-spikes and DM subhalos of DM particles χ_s with e^+e^- the dominant annihilation final states. In this scenario, the spectral shape or the width of the excess can be used to estimate the distance to the source. II) for burst-like sources with a power-law injection spectrum, the spectrum after propagation can shrink at a cooling-related cutoff energy and form a sharp spectral peak (dubbed “phase-space shrinking”). Energy-dependent diffusion also contributes to the spectral rising. Typical sources of this type are pulsar wind nebulae (PWNe) and supernova remnants (SNRs). In this scenario, the power index and the distance of the source are strongly constrained by the width of the excess.

In view of the DAMPE excess, we find: i) for the continuous sources, the favoured distance should be less than ~ 0.3 kpc. The source can be “mini-spikes” or DM subhalos with the favoured DM annihilation cross section around the typical thermal value. ii) For the burst-like source, the injection spectrum must be hard with power index significantly below two, and the distance within $\sim (3 - 4)$ kpc. The age of the source is determined to be ~ 0.16 Myr. iii) For both sources, large anisotropies in

the arrival direction of the CRE are predicted, which are close to the current Fermi-LAT upper limits. iv) We identify possible candidates for mini-spikes (PWNe) from the catalogue of Fermi-LAT 3GFL (ATNF pulsar catalogue).

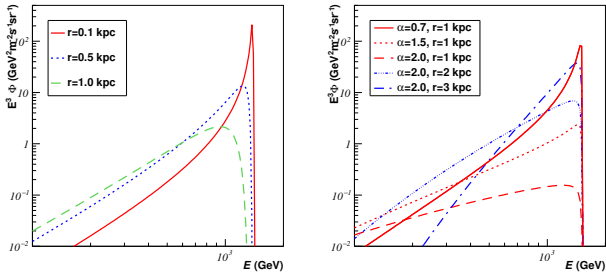


FIG. 1: Left) Effect of “spectrum broadening” on CRE flux from a continuous point-like source described in Eq. (2) with a growing distance $r = 0.1 - 1.0$ kpc. E_0 is fixed at 1.4 TeV. Right) Effect of “phase-space shrinking” for the burst-like sources in Eq. (4) with a decreasing α from 2.0 to 0.7 and fixed $r = 1$ kpc, and “energy-dependent diffusion” for a growing distance $r = 1 - 3$ kpc with fixed $\alpha = 2$. The age of the source is fixed at $t = 0.15$ Myr. For both sources, the spectra are normalized to a total flux $\Phi = 10^{-9} \text{m}^{-2} \text{s}^{-1} \text{sr}^{-1}$.

Continuous sources. The propagation of CR electrons is described by the following diffusion equation [11]

$$\frac{\partial f}{\partial t} = \frac{D(E)}{r^2} \frac{\partial}{\partial r} r^2 \frac{\partial f}{\partial r} + \frac{\partial}{\partial E} (B(E)f) + Q(r, t, E), \quad (1)$$

where $f(r, t, E)$ is the number density function per unit energy with r the distance to the source, $Q(r, t, E)$ is the source term. In the equation we have neglected the effects of convection and re-acceleration as they are only important at low energies. The energy-dependent spatial diffusion coefficient $D(E)$ is parametrized as $D(E) = D_0(E/\text{GeV})^\delta$, where $\delta = 0.31$ is a power law index and $D_0 = 5.49 \times 10^{28} \text{cm}^2 \text{s}^{-1}$ [12]. The energy-losses due to ICS processes and synchrotron radiations are parametrized as $B(E) = b_0 E^2$ with $b_0 = 1.4 \times 10^{-16} \text{GeV}^{-1} \text{s}^{-1}$ [13].

The sources of CRE can be roughly divided into continuous and burst-like sources, according to the time scale of electron injection from the sources relative to that of the propagation time. A possible continuous source is the annihilation of DM particles in the Galaxy. Very sharp δ -function-like CRE spectrum can be produced from DM annihilation directly into e^+e^- pairs in models with enhanced DM-electron coupling, or through light mediators with mass very close to twice the electron mass. However, for any continuous source, the finally observed spectrum is a superposition of electrons injected at different time. The electrons injected earlier suffer from more energy losses. Thus the superposition inevitably results in the broadening of the spectrum. For a continuous point-like source with a δ -function injection spectrum

$Q(r, E) \approx Q_0 \delta(E - E_0) \delta^{(3)}(\mathbf{r})$ with E_0 the central energy and Q_0 the normalization constant, the analytic solution to Eq. (1) is given by [14]

$$f(r, E) = \frac{Q_0 E^{-2}}{\pi^{3/2} b_0 r_d^3(E)} \exp\left(-\frac{r^2}{r_d^2(E)}\right), \quad (2)$$

where $r_d^2(E) = 4D_0[(E/\text{GeV})^{\delta-1} - (E_0/\text{GeV})^{\delta-1}]/(1 - \delta)(b_0 \text{GeV})$ is the diffusion length. As the solution shows, after the propagation, the spectrum is broadened. For $E \ll E_0$, it is an approximate power law $f \propto E^{-(1+3\delta)/2}$. The spectrum rises rapidly when E is approaching E_0 and eventually cut off exponentially at E_0 as $r_d(E) \approx 0$. In the left panel of Fig. 1, we show how the spectral shape of CRE changes with growing distance r . In the region near $E \approx E_0$ the spectral shape is very sensitive to the distance. Increasing the distance will result in a broader excess. Therefore, a precision measurement on the spectral shape can be used to determine the distance. Note that the diffusion length r_d can only set the scale of the maximal distance.

In the left panel of Fig. 2, we show the best-fit fluxes obtained from fitting to the DAMPE data for three fixed values of $r = 0.1 - 0.3$ kpc. Other parameters such as E_0 , Q_0 and the background parameters are allowed to vary in the fits. In all the three cases, the best-fit values of E_0 are quite similar $E_0 \approx 1.4 - 1.5$ TeV. With increasing value of r , the best-fit spectrum becomes broader and the fit quality becomes lower. From $r = 0.1$ to 0.3 kpc, the χ^2 -value increases from 14.2 to 19.2. The fit including r as a free parameter shows that the DAMPE data place an upper limit of $r \lesssim 0.3$ kpc at 95% C.L.. For the three cases, the best-fit values of the normalization constants are $Q_0 = (0.47 - 2.1) \times 10^{33} \text{s}^{-1}$, respectively. The detailed list of best-fit parameters and allowed regions are shown in Tab. S-2 and Fig. S-3 of the supplementary material.

Mini-spikes. One of the possible continuous point sources is the “mini-spike”, i.e., the large DM density enhancements around the intermediate mass black holes (IMBHs) with mass $\sim 10^2 - 10^6 M_\odot$ [15–18]. The IMBH can form out of popIII stars [19] or collapsing of primordial gas in early-forming halos [20]. In this letter we consider the latter case of IMBH formation. For the Milky Way-sized Galaxy, the total number of this type of IMBHs is around $\mathcal{O}(100)$ with $\sim 30\%$ of them located in the inner region $\lesssim 10$ kpc [17]. Starting from an initial NFW DM profile [21], the spiked DM profile of the mini-spike after the adiabatic growth of the IMBH follows a power law $\rho_{sp}(r) = \rho(r_{sp})(r/r_{sp})^{-\gamma_{sp}}$ where $\rho(r)$ is the initial DM profile, $r_{sp} \sim \text{pc}$ is the typical radius of the mini-spike and $\gamma_{sp} \approx 7/3$ is the power index [22]. Due to the DM annihilation, the spiked DM profile is cut off at a very small distance $r_{\text{cut}} \sim 10^{-3} \text{pc}$ [17]. Assuming Majorana DM particles χ_s which annihilate dominantly into e^+e^- pairs with velocity-averaged annihilation cross section $\langle \sigma v \rangle$, the source term of “mini-spikes” can be es-

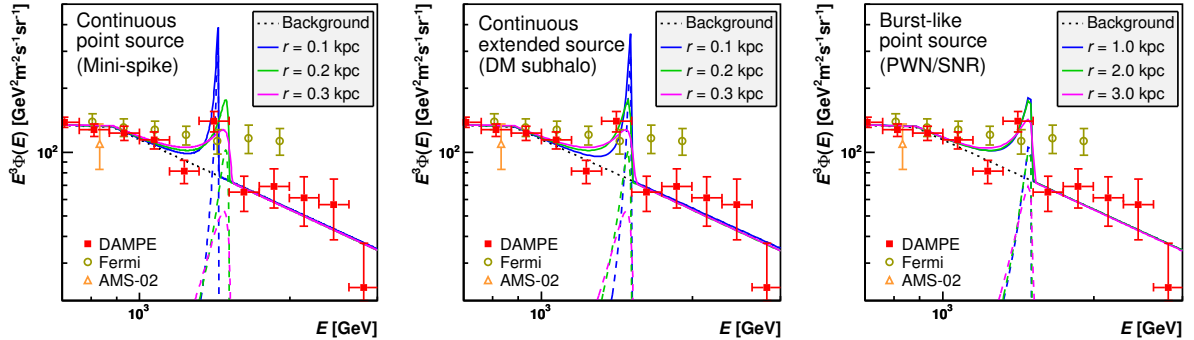


FIG. 2: Best-fit CRE flux from fitting to the DAMPE data [5] for three type of sources. Left) Continuous point-like sources (mini-spikes) with distance $r=0.1, 0.2, 0.3$ kpc, respectively. Center) Continuous extended sources (DM subhalos) for the same distances with subhalo mass fixed at $10^7 M_\odot$. Right) Burst-like sources (PWNe/SNRs) with $(r(\text{kpc}), \alpha)$ values $(1, 0.5), (2, 0.7), (3, 1.3)$, respectively. The solid (dashed) curves are the sum of the signal and background (signal only). The data of DAMPE [5], AMS-02 [2] and Ferm-LAT [3] are also shown.

timated as

$$Q_0 \approx 3.1 \times 10^{33} \text{ s}^{-1} \left(\frac{\langle \sigma v \rangle}{3 \cdot 10^{-26} \text{ cm}^3 \text{ s}^{-1}} \right) \left(\frac{1.4 \text{ TeV}}{m_\chi} \right)^2 \left(\frac{\rho(r_{sp})}{10^2 \text{ GeV cm}^{-3}} \right)^2 \left(\frac{r_{sp}}{\text{pc}} \right)^{14/3} \left(\frac{r_{cut}}{10^{-3} \text{ pc}} \right)^{-5/3}. \quad (3)$$

For the three cases of $r = 0.1 - 0.3$ kpc, using the best-fit values of Q_0 , the corresponding cross section are $\langle \sigma v \rangle = (0.48 - 2.48) \times 10^{-26} \text{ cm}^3 \text{ s}^{-1}$, which are close to the typical thermal value.

DM subhalos. It is straightforward to extend the analysis to the spatially-extended sources. N-body simulations of cold and collisionless DM predict that the Galaxy should contain large number of small subhalos [23–25]. Based on a joint analysis to the Via Lactea II and ELVIS simulations [26], we estimate that the possibility of finding a nearby subhalo within $\lesssim 1(0.3)$ kpc and total mass $M_h \gtrsim 10^6 M_\odot$ is around $\sim 1.2\%(0.03\%)$. An alternative possibility is the ultra compact mini-halos (UCMHs) formed in the early epochs of the Universe [27–30]. Finding a nearby UCMH within ~ 0.1 kpc requires that UCMHs contribute to a fraction of above $\sim 1\%$ of the total DM density [28]. In this work, we shall focus on the case of DM subhalo. As subhalos may experience a significant degree of mass loss due to tidal stripping, especially for those located at the inner volume of the Galaxy, we adopt a tidally truncated density profile $\rho(r) = \rho_0(r/\text{kpc})^{-\gamma} \exp(-r/R_b)$ [26, 31, 32]. The parameters ρ_0 , γ and R_b depend on the distance d from the center of the subhalo to the Galactic center and the total mass M_h of the subhalo, which can be extrapolated from the N-body simulation data. From the analysis in Ref. [26], we obtain $\rho_0 = 5.3 \text{ GeV} \cdot \text{cm}^{-3}$, $\gamma = 0.78$ and $R_b = 0.096 \text{ kpc}$, for a typical $M_h = 10^7 M_\odot$.

The CRE flux from the subhalo is calculated by integrating the solution of Eq. (2) over the subhalo density distribution. For $r = 0.1, 0.2, \text{ and } 0.3$ kpc, we find the best-fit annihilation cross sections $(1.04, 2.55, 4.62) \times 10^{-26} \text{ cm}^3 \text{ s}^{-1}$, respectively, which are well below the current limits on DM subhalos [26, 33, 34]. Similar to the case of point source, when r increases from 0.1 to 0.3 kpc, the best-fit spectrum becomes broader and the fit qualities become lower. The corresponding χ^2 value increases from 13.4 to 19.2. From a fit with r as a free parameter, we find that the source should be within $r \lesssim 0.3$ kpc at 95% C.L., very close to the case of mini-spikes. We also find that modifying the subhalo mass M_h does not change the conclusion. The detailed list of best-fit parameters and allowed regions are shown in Tab. S-4 and Fig. S-4 of the supplementary material. Note that for an annihilation cross section of $\mathcal{O}(10^{-26}) \text{ cm}^3 \text{ s}^{-1}$ the contribution from the whole Galactic halo DM to the CRE flux is typically two orders of magnitude smaller than that from the nearby sources, which can be safely neglected. The halo DM also contribute to extra CR positrons which could be constrained by the experiments. The constraints, however, turn out to be rather weak for TeV scale DM, as the current AMS-02 experiment only measured the positrons up to $\sim 350 \text{ GeV}$ [35] (see Fig. S-6 in the supplementary material).

Burst-like sources. For burst-like sources such as PWNe/SNRs, the injection spectrum is expected to be a broad power-law with an exponential cutoff, $Q(r, t, E) = N_0(E/\text{GeV})^{-\alpha} \exp(-E/E_c) \delta^{(3)}(\mathbf{r}) \delta(t)$, where α is the power-law index and E_c is the cutoff energy. The normalization constant N_0 can be related to the total released energy E_{tot} . The solution to the diffusion equa-

tion Eq. (1) for this type of source is given by [14]

$$f(r, E) = \frac{N_0(E/\text{GeV})^{-\alpha}}{\pi^{3/2}r_d^3} \xi(E)^{\alpha-2} \exp\left(-\frac{r^2}{r_d^2} - \frac{E}{\xi(E)E_c}\right), \quad (4)$$

where $\xi(E) = 1 - E/E_{\text{max}}$ with $E_{\text{max}} = (b_0t)^{-1}$ the maximal possible energy of an electron from a source of age t . The diffusion length for this type of source is $r_d(E) = 2\sqrt{\lambda(E)D(E)t}$, where $\lambda(E) = [1 - \xi(E)^{1-\delta}]/(1-\delta)(1 - \xi(E))$. For $E \ll E_{\text{max}}$, $r_d(E) \approx 2\sqrt{D(E)t}$. While the value of α is commonly considered to be ~ 2 , the cutoff E_c is poorly constrained. We shall focus on the large cutoff limit, i.e. $E_c \gg E_{\text{max}}$. In this case, E_{max} will play the role of spectral cutoff instead of E_c , namely, a cooling cutoff will appear, as can be seen in Eq. (4).

In this work, we emphasize that for the burst-like source a sharp spectral rise near the cutoff energy E_{max} can appear for some choices of α and r for two reasons: **i)** Cooling related “phase-space shrinking”. An initial electron with energy E_s at time $t = 0$ is related to its energy E observed at later time t as $E_s = E/\xi(E)$. Thus an initial energy interval ΔE_s will shrink to $\Delta E = \xi(E)^2 \Delta E_s$ at time t . Since the number of electrons is unchanged during cooling, the energy spectrum at time t is $\Delta N/\Delta E \approx E^{-\alpha} \xi(E)^{\alpha-2}$. For a relatively hard spectrum with $\alpha < 2$, the shrinking of phase space can enhance the number density. Since $\xi(E)$ vanishes when E is approaching E_{max} , the shrinking of phase space leads to a rapid rise of the energy spectrum. This effect of “phase-space shrinking” is illustrated in the right panel of Fig. 1. The DAMPE data suggest that the cutoff should be in the range $E_{\text{max}} \approx 1.3 - 1.5$ TeV, which in turn sets the age of the source $t \approx (0.15 - 0.17)$ Myr, and the diffusion length at E_{max} , $r_d(E_{\text{max}}) \approx (0.79 - 0.84)$ kpc. **ii)** “Energy-dependent diffusion” which is related to the fact that for $\delta > 0$, higher energy electrons have larger diffusion coefficients. The energy dependence in the exponential factor of Eq. (4) can be written as $\exp(-r^2/r_d^2) \approx \exp[-\kappa^2(E/E_{\text{max}})^{-\delta}]$ where $\kappa = r^2/r_d^2(E_{\text{max}})$. For relatively large distance $\kappa > 1$, the energy-dependent factor also contributes to the rising of the spectrum near E_{max} , which is illustrated in Fig. 1. Of course, in order to compensate the exponential suppression of the flux at large κ , the normalization constant N_0 or E_{tot} has to be large enough. The reasonable value of E_{tot} should be smaller than the typical kinetic energy carried by SNR or the total energy of supernova explosion of $\sim (10^{51} - 10^{53})$ erg, which sets the scale of the distance of the sources.

In general, unconventional values of α which is significantly smaller than ~ 2 is required to reproduce the DAMPE excess, especially for small r . In the right panel of Fig. 2 we show the best-fit spectra for three typical combinations of r (in kpc) and α with $(r, \alpha) = (1, 0.5)$, $(2, 0.7)$ and $(3, 1.3)$, respectively. A scan in the (r, α) parameter space shows that in the region $r < r_d$, the

allowed α has to be very small $\alpha \lesssim 0.65$. In the region $r > r_d$ the value of α can reach at most 1.4 at 3 kpc, as the effect of energy-dependent diffusion is significant. By imposing the condition of $E_{\text{tot}} < 10^{51} (10^{53})$ erg, the distance r is restricted in the range $r \lesssim 3(4)$ kpc. Together with the required age of the source, we find 7 candidate pulsars with $r \lesssim 4$ kpc in the ATNF catalog of pulsars [36]: B0740-28, J0922-4949, J1055-6022, J1151-6108, J1509-5850, J1616-5017 and J1739-3023. Distances of the sources lie in the range (2.0–3.6) kpc. In this region, both the effects of “phase-space shrinking” and “energy-dependent diffusion” are relevant. The detailed list of best-fit parameters, allowed regions and the list of the candidate pulsars are shown in Tab. S-6, Fig. S-7 and Tab. S-7 of the supplementary material. For both continuous and burst-like sources, varying the propagation parameters D_0 and δ within uncertainties ($\sim 20\%$ for D_0 and $\sim 10\%$ for δ as determined in [12]) mainly results in the changes in the over all normalization factors Q_0 and N_0 up to $\sim 30\%$.

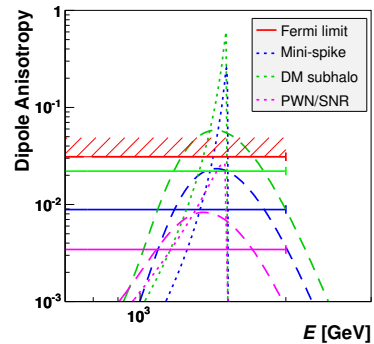


FIG. 3: Predictions for electron anisotropies corresponding to a selection of the cases considered in Fig. 2: i) the continuous point-like source (mini-spike) with $r = 0.2$ kpc (dashed blue); ii) the continuous extended source (subhalo) with $r = 0.2$ kpc and $M_h = 10^7 M_\odot$ (dashed green); iii) the burst-like source (PWN/SNR) with $r = 2$ kpc and $\alpha = 0.7$ (dashed magenta). The solid curves with the same color correspond to the anisotropies convoluted with an energy resolution of 15%. The current upper limits from Fermi-LAT in the energy interval 0.55–2 TeV (using the method of shuffling technique) are also shown [37].

Anisotropies. Nearby sources can generate non-negligible anisotropy in the CRE flux. For an illustration, we show in Fig. 3 the predicted dipole anisotropies from the sources as a function of the CRE energy, corresponding to one of the parameter sets considered in each type of the sources shown in Fig. 2. Assuming a perfect energy resolution of the detector, large anisotropies of $\mathcal{O}(10^{-1})$ with sharp structures are predicted. The anisotropies in continuous sources are in general larger than that in the burst-like sources, which is related to the relatively small

diffusion length. The Fermi-LAT has reported upper limits on the dipole anisotropy of $\lesssim 3 \times 10^{-2}$ at 95% C.L. over the energy interval 0.55–2 TeV [37]. Note that the energy resolution of Fermi-LAT is $\sim 10\%$ (17%) at 1 (2) TeV. In Fig. 3, we also show the predicted anisotropies convoluted with an energy resolution of 15%. After the convolution, the predicted anisotropies are smaller and can reach $\mathcal{O}(10^{-2})$, which is comparable with the current Fermi-LAT limits. Note that a quantitative comparison with the data requires a reliable estimation of the anisotropies contributed by the backgrounds which can easily reach $\mathcal{O}(10^{-3} - 10^{-2})$ alone, but depends strongly on the assumed spatial distribution of the astrophysical sources [38].

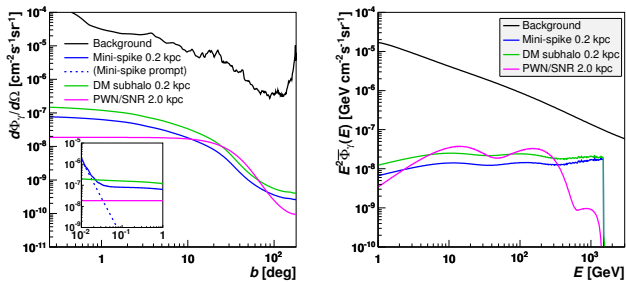


FIG. 4: Predictions for the Galactic diffuse γ -ray fluxes in the three cases considered in Fig. 3 assuming the direction of the sources is coincide with the GC. Left) $d\Phi_\gamma/d\Omega$ as a function of Galactic latitude b along the direction of $\ell = 0^\circ$. The inset shows the fluxes in the inner region, which indicates that the γ -rays from the mini-spike increase sharply towards low b due to prompt photons from DM annihilation, making it appears as a point-like source. Right) Energy spectra of γ -ray fluxes averaged over a circular region with radius 30° centered at the GC. The Galactic diffuse γ -ray background is calculated using GALPROP-v54 [39] with a reference propagation model adopted by Fermi-LAT [40]. The ISRF in the solar neighbourhood is interpolated from Ref. [41].

Gamma-ray signals. DM annihilation can produce prompt photons through final state radiation (FSR) of charged leptons. The FSR photon spectrum has a distinct feature of an approximate power law with index ~ 1 for $E \ll m_\chi$, plus a sharp cutoff at m_χ . In morphology, mini-spikes appear as point-like sources due to the high concentration of DM density. For the cases of mini-spike considered in Fig. 2, the total fluxes ($E > 1$ GeV) are in the range $\sim (0.71 - 1.51) \times 10^{-10} \text{ cm}^{-2} \text{ s}^{-1}$. In the Fermi-LAT 3FGL catalogue of unassociated point sources [42], we find 6 candidate sources with low power indices which can reach ~ 1 within 2σ error: J0603.3+2042, J1250.2-0233, J2209.8-0450, J1705.5-4128c, J2142.6-2029 and J2300.0+4053. Most of them have total fluxes of $\mathcal{O}(10^{-10}) \text{ cm}^{-2} \text{ s}^{-1}$ which are consistent with that favoured by the mini-spikes. The favoured DM annihilation cross sections for both mini-spikes and DM subhalos

are well below the current upper limits derived from the γ rays towards dwarf Galaxies [43] and the Galactic center (GC) [44] under the assumption of smooth DM profiles. Taking into account the distribution of mini-spikes, very stringent constraints on the annihilation cross sections were obtained by HESS from the GC γ -ray data [45], which are highly model dependent. The γ -rays constraints from other sky regions are much weaker [46].

All the CRE sources can produce diffuse γ -rays through electron inverse Compton scattering (ICS) off interstellar radiation fields (ISRF), the corresponding energy spectrum is softer compared with that of the FSR photons [47]. For the typical parameters considered in the three scenarios in Fig. 2, the predicted differential flux $E^3 d\Phi/dE$ can reach $\mathcal{O}(10^{-8}) \text{ GeV cm}^{-2} \text{ s}^{-1} \text{ sr}^{-1}$ in the energy range $\sim (0.1 - 1)$ TeV, which may be subject to the constraints from the Fermi-LAT data on the Galactic diffuse γ -rays [48]. However, the Fermi-LAT constraints vary with sky regions. In the low Galactic latitudes regions the backgrounds can easily reach $\sim 10^{-6} \text{ GeV cm}^{-2} \text{ s}^{-1} \text{ sr}^{-1}$ and dominate the total diffuse γ -ray emission. In this case the Fermi-LAT data cannot place stringent constraints on these CRE sources. This possibility is illustrated in Fig. 4, where the direction of the source is assumed to coincide with the GC. For the three cases discussed in Fig. 3, we show the spatial extension as well as the energy spectrum of the associated γ -rays, together with the corresponding Galactic diffuse γ -ray backgrounds. In the calculations, the contributions from the Galactic halo DM for mini-spikes and DM subhalos are included assuming an Einasto DM profile. The Galactic diffuse γ -ray background is calculated using a reference propagation model adopted by Fermi-LAT [40] which agrees with the data well. It can be seen that for the typical parameters considered, the predicted γ -ray fluxes can be a few orders of magnitude below the background, which suggests that the Ferm-LAT constraints should be rather weak, as the uncertainties in the background model are still significant (see the supplementary material for detailed calculations on the diffuse γ -rays).

This work is supported in part by the National Key R&D Program of China No. 2017YFA0402204, the NSFC under Grants No. 11335012, 11690022, 11475237 and U1738209, and the CAS Key Research Programs, No. XDB23030100 and QYZDY-SSW-SYS007. *Note added.* After submitting the first version of the manuscript, a number of analyses on the DAMPE data appeared [49–85]. We found that most of the proposed models fall into the scenarios discussed in our work. Ref. [49] discussed the contributions from PWNe and DM substructures. Their conclusions are also consistent with ours.

- [1] C. Shen, *Astrophys. J.* **162**, L181 (1970).
- [2] M. Aguilar *et al.* (AMS), *Phys. Rev. Lett.* **113**, 221102 (2014).
- [3] S. Abdollahi *et al.* (Fermi-LAT), *Phys. Rev.* **D95**, 082007 (2017), [arXiv:1704.07195 \[astro-ph.HE\]](#) .
- [4] O. Adriani *et al.* (CALET), *Phys. Rev. Lett.* **119**, 181101 (2017), [arXiv:1712.01711 \[astro-ph.HE\]](#) .
- [5] J. Chang (DAMPE), *Nature* , DOI:10.1038/nature24475 (2017), [1711.10981](#) .
- [6] F. Aharonian *et al.* (H.E.S.S.), *Phys. Rev. Lett.* **101**, 261104 (2008), [arXiv:0811.3894 \[astro-ph\]](#) .
- [7] F. Aharonian *et al.* (H.E.S.S.), *Astron. Astrophys.* **508**, 561 (2009), [arXiv:0905.0105 \[astro-ph.HE\]](#) .
- [8] D. Kerszberg (H.E.S.S.), Talk at ICRC2017 (2017).
- [9] D. Borla Tridon, P. Colin, L. Cossio, M. Doro, and V. Scalzotto (MAGIC), in *Proceedings, ICRC 2011, Beijing*, Vol. 6 (2011) pp. 47–50, [arXiv:1110.4008 \[astro-ph.HE\]](#) .
- [10] D. Staszak (VERITAS), *Proceedings, 34th International Cosmic Ray Conference (ICRC 2015): The Hague, The Netherlands, July 30-August 6, 2015*, PoS **ICRC2015**, 411 (2016), [34,411(2015)], [arXiv:1508.06597 \[astro-ph.HE\]](#) .
- [11] V. L. Ginzburg and S. I. Syrovatskii, “The origin of cosmic rays (pergamon, oxford, 1964),” .
- [12] R. Trotta, G. Johannesson, I. V. Moskalenko, T. A. Porter, R. R. de Austri, and A. W. Strong, *Astrophys. J.* **729**, 106 (2011), [arXiv:1011.0037 \[astro-ph.HE\]](#) .
- [13] T. Linden and S. Profumo, *Astrophys. J.* **772**, 18 (2013), [arXiv:1304.1791 \[astro-ph.HE\]](#) .
- [14] A. M. Atoian, F. A. Aharonian, and H. J. Volk, *Phys. Rev.* **D52**, 3265 (1995).
- [15] M. C. Miller and E. J. M. Colbert, *Int. J. Mod. Phys.* **D13**, 1 (2004), [arXiv:astro-ph/0308402 \[astro-ph\]](#) .
- [16] H.-S. Zhao and J. Silk, *Phys. Rev. Lett.* **95**, 011301 (2005), [arXiv:astro-ph/0501625 \[astro-ph\]](#) .
- [17] G. Bertone, A. R. Zentner, and J. Silk, *Phys. Rev.* **D72**, 103517 (2005), [arXiv:astro-ph/0509565 \[astro-ph\]](#) .
- [18] G. Bertone, M. Fornasa, M. Taoso, and A. R. Zentner, *New J. Phys.* **11**, 105016 (2009), [arXiv:0905.4736 \[astro-ph.HE\]](#) .
- [19] A. Heger, C. L. Fryer, S. E. Woosley, N. Langer, and D. H. Hartmann, *Astrophys. J.* **591**, 288 (2003), [arXiv:astro-ph/0212469 \[astro-ph\]](#) .
- [20] S. M. Koushiappas, J. S. Bullock, and A. Dekel, *Mon. Not. Roy. Astron. Soc.* **354**, 292 (2004), [arXiv:astro-ph/0311487 \[astro-ph\]](#) .
- [21] J. F. Navarro, C. S. Frenk, and S. D. M. White, *Astrophys. J.* **490**, 493 (1997), [arXiv:astro-ph/9611107 \[astro-ph\]](#) .
- [22] P. Gondolo and J. Silk, *Phys. Rev. Lett.* **83**, 1719 (1999), [arXiv:astro-ph/9906391 \[astro-ph\]](#) .
- [23] V. Springel, J. Wang, M. Vogelsberger, A. Ludlow, A. Jenkins, A. Helmi, J. F. Navarro, C. S. Frenk, and S. D. M. White, *Mon. Not. Roy. Astron. Soc.* **391**, 1685 (2008), [arXiv:0809.0898 \[astro-ph\]](#) .
- [24] J. Diemand, M. Kuhlen, P. Madau, M. Zemp, B. Moore, D. Potter, and J. Stadel, *Nature* **454**, 735 (2008), [arXiv:0805.1244 \[astro-ph\]](#) .
- [25] S. Garrison-Kimmel, M. Boylan-Kolchin, J. Bullock, and K. Lee, *Mon. Not. Roy. Astron. Soc.* **438**, 2578 (2014), [arXiv:1310.6746 \[astro-ph.CO\]](#) .
- [26] D. Hooper and S. J. Witte, *JCAP* **1704**, 018 (2017), [arXiv:1610.07587 \[astro-ph.HE\]](#) .
- [27] M. Ricotti and A. Gould, *Astrophys. J.* **707**, 979 (2009), [arXiv:0908.0735 \[astro-ph.CO\]](#) .
- [28] P. Scott and S. Sivertsson, *Phys. Rev. Lett.* **103**, 211301 (2009), [Erratum: *Phys. Rev. Lett.*105,119902(2010)], [arXiv:0908.4082 \[astro-ph.CO\]](#) .
- [29] A. S. Josan and A. M. Green, *Phys. Rev.* **D82**, 083527 (2010), [arXiv:1006.4970 \[astro-ph.CO\]](#) .
- [30] T. Bringmann, P. Scott, and Y. Akrami, *Phys. Rev.* **D85**, 125027 (2012), [arXiv:1110.2484 \[astro-ph.CO\]](#) .
- [31] S. Kazantzidis, L. Mayer, C. Mastroiello, J. Diemand, J. Stadel, and B. Moore, *Astrophys. J.* **608**, 663 (2004), [arXiv:astro-ph/0312194 \[astro-ph\]](#) .
- [32] J. Penarrubia, J. F. Navarro, and A. W. McConnachie, *Astrophys. J.* **673**, 226 (2008), [arXiv:0708.3087 \[astro-ph\]](#) .
- [33] A. Albert *et al.* (DES, Fermi-LAT), *Astrophys. J.* **834**, 110 (2017), [arXiv:1611.03184 \[astro-ph.HE\]](#) .
- [34] D. Schoonenberg, J. Gaskins, G. Bertone, and J. Diemand, *JCAP* **1605**, 028 (2016), [arXiv:1601.06781 \[astro-ph.HE\]](#) .
- [35] L. Accardo *et al.* (AMS), *Phys. Rev. Lett.* **113**, 121101 (2014).
- [36] R. N. Manchester, G. B. Hobbs, A. Teoh, and M. Hobbs, *Astron. J.* **129**, 1993 (2005), [arXiv:astro-ph/0412641 \[astro-ph\]](#) .
- [37] S. Abdollahi *et al.* (Fermi-LAT), *Phys. Rev. Lett.* **118**, 091103 (2017), [arXiv:1703.01073 \[astro-ph.HE\]](#) .
- [38] S. Manconi, M. Di Mauro, and F. Donato, *JCAP* **1701**, 006 (2017), [arXiv:1611.06237 \[astro-ph.HE\]](#) .
- [39] GALPROP, “<https://galprop.stanford.edu>,” .
- [40] M. Ackermann *et al.* (Fermi-LAT), *Astrophys. J.* **750**, 3 (2012), [arXiv:1202.4039 \[astro-ph.HE\]](#) .
- [41] T. A. Porter, I. V. Moskalenko, A. W. Strong, E. Orlando, and L. Bouchet, *Astrophys. J.* **682**, 400 (2008), [arXiv:0804.1774 \[astro-ph\]](#) .
- [42] F. Acero *et al.* (Fermi-LAT), *Astrophys. J. Suppl.* **218**, 23 (2015), [arXiv:1501.02003 \[astro-ph.HE\]](#) .
- [43] M. Ackermann *et al.* (Fermi-LAT), *Phys. Rev. Lett.* **115**, 231301 (2015), [arXiv:1503.02641 \[astro-ph.HE\]](#) .
- [44] H. Abdallah *et al.* (H.E.S.S.), *Phys. Rev. Lett.* **117**, 111301 (2016), [arXiv:1607.08142 \[astro-ph.HE\]](#) .
- [45] F. Aharonian *et al.* (H.E.S.S.), *Phys. Rev.* **D78**, 072008 (2008), [arXiv:0806.2981 \[astro-ph\]](#) .
- [46] T. Bringmann, J. Lavalle, and P. Salati, *Phys. Rev. Lett.* **103**, 161301 (2009), [arXiv:0902.3665 \[astro-ph.CO\]](#) .
- [47] P. Meade, M. Papucci, A. Strumia, and T. Volansky, *Nucl. Phys.* **B831**, 178 (2010), [arXiv:0905.0480 \[hep-ph\]](#) .
- [48] M. Ackermann *et al.* (Fermi-LAT), *Astrophys. J.* **761**, 91 (2012), [arXiv:1205.6474 \[astro-ph.CO\]](#) .
- [49] Q. Yuan *et al.*, (2017), [arXiv:1711.10989 \[astro-ph.HE\]](#) .
- [50] Y.-Z. Fan, W.-C. Huang, M. Spinrath, Y.-L. S. Tsai, and Q. Yuan, (2017), [arXiv:1711.10995 \[hep-ph\]](#) .
- [51] K. Fang, X.-J. Bi, and P.-F. Yin, (2017), [arXiv:1711.10996 \[astro-ph.HE\]](#) .
- [52] G. H. Duan, L. Feng, F. Wang, L. Wu, J. M. Yang, and R. Zheng, (2017), [arXiv:1711.11012 \[hep-ph\]](#) .
- [53] P.-H. Gu and X.-G. He, (2017), [arXiv:1711.11000 \[hep-ph\]](#) .
- [54] P. Athron, C. Balazs, A. Fowlie, and Y. Zhang, (2017), [arXiv:1711.11376 \[hep-ph\]](#) .

- [55] J. Cao, L. Feng, X. Guo, L. Shang, F. Wang, and P. Wu, (2017), [arXiv:1711.11452 \[hep-ph\]](#) .
- [56] X. Liu and Z. Liu, (2017), [arXiv:1711.11579 \[hep-ph\]](#) .
- [57] L. Zu, C. Zhang, L. Feng, Q. Yuan, and Y.-Z. Fan, (2017), [arXiv:1711.11052 \[hep-ph\]](#) .
- [58] Y.-L. Tang, L. Wu, M. Zhang, and R. Zheng, (2017), [arXiv:1711.11058 \[hep-ph\]](#) .
- [59] W. Chao and Q. Yuan, (2017), [arXiv:1711.11182 \[hep-ph\]](#) .
- [60] P.-H. Gu, (2017), [arXiv:1711.11333 \[hep-ph\]](#) .
- [61] G. H. Duan, X.-G. He, L. Wu, and J. M. Yang, (2017), [arXiv:1711.11563 \[hep-ph\]](#) .
- [62] I. Cholis, T. Karwal, and M. Kamionkowski, (2017), [arXiv:1712.00011 \[astro-ph.HE\]](#) .
- [63] H.-B. Jin, B. Yue, X. Zhang, and X. Chen, (2017), [arXiv:1712.00362 \[astro-ph.HE\]](#) .
- [64] Y. Gao and Y.-Z. Ma, (2017), [arXiv:1712.00370 \[astro-ph.HE\]](#) .
- [65] J.-S. Niu, T. Li, R. Ding, B. Zhu, H.-F. Xue, and Y. Wang, (2017), [arXiv:1712.00372 \[astro-ph.HE\]](#) .
- [66] W. Chao, H.-K. Guo, H.-L. Li, and J. Shu, (2017), [arXiv:1712.00037 \[hep-ph\]](#) .
- [67] C.-H. Chen, C.-W. Chiang, and T. Nomura, (2017), [arXiv:1712.00793 \[hep-ph\]](#) .
- [68] T. Li, N. Okada, and Q. Shafi, (2017), [arXiv:1712.00869 \[hep-ph\]](#) .
- [69] R. Zhu and Y. Zhang, (2017), [arXiv:1712.01143 \[hep-ph\]](#) .
- [70] P.-H. Gu, (2017), [arXiv:1712.00922 \[hep-ph\]](#) .
- [71] T. Nomura and H. Okada, (2017), [arXiv:1712.00941 \[hep-ph\]](#) .
- [72] K. Ghorbani and P. H. Ghorbani, (2017), [arXiv:1712.01239 \[hep-ph\]](#) .
- [73] J. Cao, L. Feng, X. Guo, L. Shang, F. Wang, P. Wu, and L. Zu, (2017), [arXiv:1712.01244 \[hep-ph\]](#) .
- [74] F. Yang and M. Su, (2017), [arXiv:1712.01724 \[astro-ph.HE\]](#) .
- [75] R. Ding, Z.-L. Han, L. Feng, and B. Zhu, (2017), [arXiv:1712.02021 \[hep-ph\]](#) .
- [76] G.-L. Liu, F. Wang, W. Wang, and J. M. Yang, (2017), [arXiv:1712.02381 \[hep-ph\]](#) .
- [77] S.-F. Ge and H.-J. He, (2017), [arXiv:1712.02744 \[astro-ph.HE\]](#) .
- [78] Y. Zhao, K. Fang, M. Su, and M. C. Miller, (2017), [arXiv:1712.03210 \[astro-ph.HE\]](#) .
- [79] Y. Sui and Y. Zhang, (2017), [arXiv:1712.03642 \[hep-ph\]](#) .
- [80] N. Okada and O. Seto, (2017), [arXiv:1712.03652 \[hep-ph\]](#) .
- [81] J. Cao, X. Guo, L. Shang, F. Wang, and P. Wu, (2017), [arXiv:1712.05351 \[hep-ph\]](#) .
- [82] B. Dutta, T. Kamon, P. Ko, and J. Li, (2017), [arXiv:1712.05123 \[hep-ph\]](#) .
- [83] A. Fowlie, (2017), [arXiv:1712.05089 \[hep-ph\]](#) .
- [84] Z.-L. Han, W. Wang, and R. Ding, (2017), [arXiv:1712.05722 \[hep-ph\]](#) .
- [85] J.-S. Niu, T. Li, and F.-Z. Xu, (2017), [arXiv:1712.09586 \[hep-ph\]](#) .

SUPPLEMENTARY MATERIAL

Origins of sharp cosmic-ray electron structures and the DAMPE excess

Xian-Jun Huang, Yue-Liang Wu, Wei-Hong Zhang, and Yu-Feng Zhou

In this supplementary material, we give more details and discussions of the results obtained in the letter.

A. Properties of the DAMPE excess

We adopt a two-component description of the CRE flux, namely, the main bulk of the CRE flux arises from distant astrophysical sources in the Galaxy, which leads to a smooth power law-like background. In addition, there is a dominant nearby source of high energy CRE which contributes to an excess over the smooth background. To estimate the significance of the DAMPE excess, we consider a reference background model in which the flux Φ_b is assumed to be a broken power law $\Phi_b(E) = N_b(E/E_{\text{brk}})^{-\gamma}$, where $\gamma = \gamma_{1(2)}$ for the electron energy below (above) a break energy E_{brk} , and N_b is a normalization factor. The flux of the excess is parametrized as Gaussian $\Phi_s(E) = N_s \exp[-(E - \mu)^2/2\sigma^2]$, where μ and σ are the central value and half-width, respectively, and N_s is a normalization factor. We fit to the DAMPE data in the energy interval 55 GeV–4.6 TeV. In total 32 data points are included. The model parameters are determined through minimizing the χ^2 -function defined as follows

$$\chi^2 = \sum_i \frac{(\Phi_{b,i} + \Phi_{s,i} - \Phi_{\text{exp},i})^2}{\sigma_{\text{exp},i}^2}, \quad (\text{S-1})$$

where $\Phi_{b(s),i}$ is the theoretical value of the background (excess) *averaged* over the width of the i -th energy bin, $\Phi_{\text{exp},i}$ and σ_i are the measured mean value and error of the flux in the energy bin. The effect of finite energy resolution is neglected as the energy resolution of DAMPE is quite high, better than 1.5% at 800 GeV. The minimization of χ^2 is performed using the MINUIT package. The fit results in the scenarios of background-only and background plus the excess are summarized in Tab. S-1. It can be seen that in the background-only scenario while the power index γ_1 is well constrained with uncertainty within $\sim 0.3\%$, the uncertainty in γ_2 is much larger around $\sim 5\%$, which is due to the limited statistics at high energies. Compared with the background-only scenario, the inclusion of a Gaussian excess leads to a reduction of $\Delta\chi^2 = 13.7$, roughly corresponding to $\sim 3.7\sigma$ local significance. Since the excess is observed in a single energy bin, the lower limit of the width σ cannot be determined, namely, the possibility of an electron-line is not ruled out for the moment. We find that at 68% (95%) C.L., the upper limit on the width is $\sigma \leq 60.4$ (89.6) GeV. In Fig. S-1, we show the best-fit fluxes for fixed $\sigma = 20, 60$ and 90 GeV, the corresponding χ^2 values are 12.2, 13.2 and 16.2, respectively.

	E_{brk} (GeV)	γ_1	γ_2	N_b	μ (GeV)	σ (GeV)	N_s	$\chi^2/\text{d.o.f.}$
background-only	884_{-93}^{+93}	3.10 ± 0.01	$3.95_{-0.16}^{+0.19}$	$1.91_{-0.52}^{+0.81}$	25.85/28
background+excess	863_{-90}^{+74}	3.10 ± 0.01	$4.03_{-0.18}^{+0.19}$	$2.06_{-0.48}^{+0.86}$	$1418.2_{-99.9}^{+95.4}$	$0_{-0.0}^{+60.36}$	0.643	12.18/25

TAB. S-1: Best-fit parameters in the scenarios of background-only and background plus a Gaussian excess. The normalization constants N_b, N_s are in units of $10^{-7} \text{ GeV}^{-1} \text{ m}^{-2} \text{ s}^{-1} \text{ sr}^{-1}$.

B. Continuous sources

Point-like sources

The fit results for the scenarios of continuous point-like sources for three representative choices of distances $r = 0.1, 0.2$ and 0.3 kpc, together with the best-fit background parameters are summarized in Tab. S-2, where the break energy of the background is fixed at the best-fit value in the background-only scenario, i.e., $E_{\text{brk}} = 884$ GeV. The propagation parameters D_0, δ and b_0 are given in the letter. In the case where the distance r is allowed to vary freely, the value of χ^2 decrease with decreasing r and gradually reaches a minimal value $\chi_{\text{min}}^2 = 13.0$ in the limit $r \rightarrow 0$. This result is again related to the fact that the excess is observed in a single energy bin and the χ^2 value is based on the

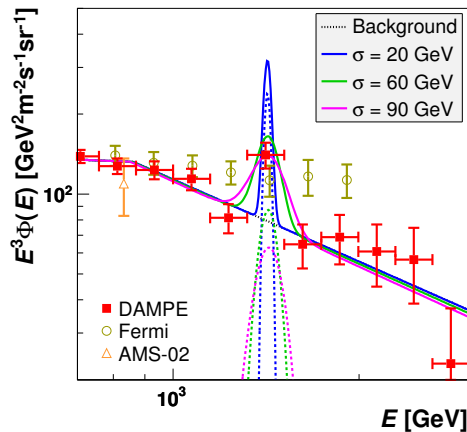


FIG. S-1: Best-fit energy spectra in the scenarios of background-only and the background plus a Gaussian signal with width $\sigma = 20, 60$ and 90 GeV, respectively. The data of AMS-02 [2], Ferm-LAT [3], and DAMPE [4] are also shown.

r [kpc]	Q_0 (10^{32} s^{-1})	E_0 (GeV)	γ_1	γ_2	N_b	$\chi^2/\text{d.o.f.}$
0.1	$4.67^{+1.39}_{-1.48}$	1446^{+32}_{-77}	3.10 ± 0.01	$4.08^{+0.14}_{-0.13}$	1.90 ± 0.03	14.18/27
0.2	$11.84^{+3.82}_{-4.00}$	1525^{+34}_{-19}	3.10 ± 0.01	$4.09^{+0.15}_{-0.13}$	1.90 ± 0.03	15.81/27
0.3	$20.78^{+8.28}_{-8.62}$	1554^{+34}_{-33}	3.10 ± 0.01	$4.09^{+0.16}_{-0.14}$	$1.89^{+0.03}_{-0.04}$	19.15/27

TAB. S-2: Best-fit parameters for continuous point-like sources with distance $r=0.1, 0.2$ and 0.3 kpc. The normalization constant N_b is in units of $10^{-7} \text{GeV}^{-1} \text{m}^{-2} \text{s}^{-1} \text{sr}^{-1}$. The best-fit values of Q_0 correspond to the DM annihilation cross section $\langle\sigma v\rangle = 4.82 \times 10^{-27}, 1.36 \times 10^{-26},$ and $2.48 \times 10^{-26} \text{cm}^3 \text{s}^{-1}$ for $r = 0.1, 0.2$ and 0.3 kpc, respectively.

bin-average. We thus define the allowed regions in (r, E_0) and (r, Q_0) planes at 68% (95%) C.L. for two parameters, corresponding to $\Delta\chi^2 = 2.3$ (5.99), which are shown in Fig. S-2. It can be seen that the allowed distance is constrained to be $r \lesssim 0.3$ kpc at 95% C.L. The value of E_0 is constrained in the 1.35 – 1.55 TeV range which is compatible with the width of the excess.

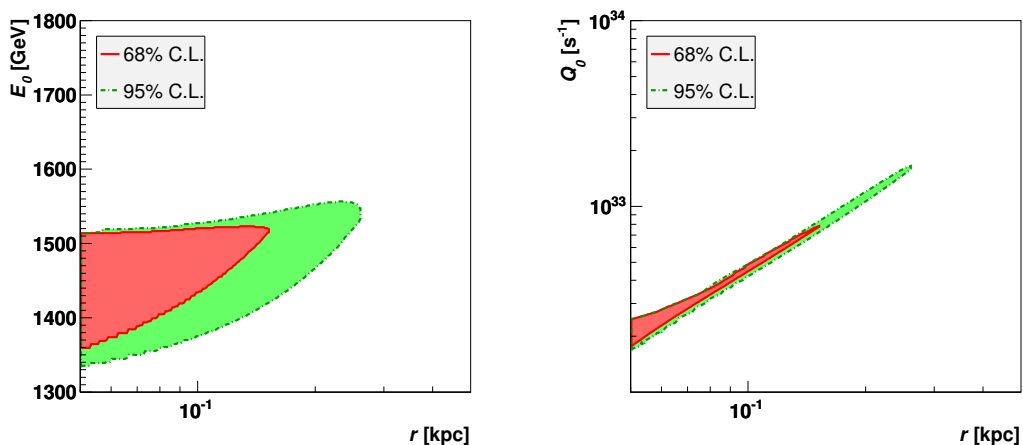


FIG. S-2: Left) Allowed regions at 68% and 95% C.Ls. in (r, E_0) plane for continuous point-like sources. Right) The same as Left, but for the allowed regions in (r, Q_0) plane.

Mini-spikes

We consider the scenario of IMBHs originated from massive objects formed directly during the collapse of primordial gas (pGas) in early-forming halos. The initial DM profile of the halo prior to the adiabatic growth of the blackhole is assumed to be NFW [20]

$$\rho(r) = \frac{\rho_s}{\left(\frac{r}{r_s}\right)^\gamma \left(1 + \frac{r}{r_s}\right)^{3-\gamma}}, \quad (\text{S-2})$$

where ρ_s and r_s are reference energy density and distance, respectively. γ is the inner slope of the profile, and in the standard NFW profile $\gamma = 1$. After the adiabatic growth of the blackhole, the spiked profile is a power law[21]

$$\rho_{sp}(r) = \rho(r_{sp}) \left(\frac{r}{r_{sp}}\right)^{-\gamma_{sp}}, \quad (\text{S-3})$$

where $r_{sp} \sim \text{pc}$ and $\gamma_{sp} = (9 - 2\gamma)/(4 - \gamma)$. For $\gamma = 1$, $\gamma_{sp} = 7/3$. The spiked DM profile is apparently divergent at small radii. However, the DM annihilation sets an upper limit ρ_{lim} on the DM density of order $\rho_{\text{lim}} = \rho_{sp}(r_{\text{lim}}) \approx m_\chi / \langle \sigma v \rangle t$ with t the age of the mini-spike. Thus $\rho_{sp}(r)$ should have an inner cut-off at radius r_{cut} , which is defined as $r_{\text{cut}} = \max\{4R_{\text{Schw}}, r_{\text{lim}}\}$, where R_{Schw} is the Schwarzschild radius of the IMBH. For typical value of $r_{\text{lim}} \approx 10^{-3}$ pc, which is larger than the typical Schwarzschild radius $R_{\text{Schw}} \approx 2.95$ km (M_{bh}/M_\odot). Thus we take $r_{\text{cut}} = r_{\text{lim}}$. The source term from the annihilation of Majorana DM particles (with mass m_χ) directly into e^+e^- can be written as

$$Q_e(E) = \frac{N_e \langle \sigma v \rangle}{2m_\chi^2} \delta(E - E_0) \int_{r_{\text{cut}}}^{r_{sp}} \rho_{sp}^2(r') 4\pi r'^2 dr', \quad (\text{S-4})$$

where $N_e = 2$ is the number of CRE per DM annihilation, and $E_0 = m_\chi$. After integrating over r' , the source term can be written as

$$Q_e(E) = \frac{N_e \langle \sigma v \rangle L}{2m_\chi^2} \delta(E - E_0), \quad (\text{S-5})$$

where L is the annihilation luminosity

$$L \equiv \int_{r_{\text{cut}}}^{r_{sp}} \rho_{sp}^2(r') 4\pi r'^2 dr' = \frac{4\pi r_{sp}^3}{2\gamma_{sp} - 3} \rho^2(r_{sp}) \left(\frac{r_{\text{cut}}}{r_{sp}}\right)^{3-2\gamma_{sp}}. \quad (\text{S-6})$$

In the case of $\gamma_{sp} = 7/3$, it can be written as

$$Q_e(E) = \frac{6\pi N_e \langle \sigma v \rangle}{5m_\chi^2} \rho^2(r_{sp}) r_{sp}^{14/3} r_{\text{cut}}^{-5/3} \delta(E - E_0), \quad (\text{S-7})$$

which leads to the expression of Eq. (3) in the letter.

DM subhalos

The DM subhalos located at the inner volume of the Galaxy may experience a significant degree of mass loss due to tidal stripping, as they encounter other subhalos more frequently. Therefore we adopt a tidally truncated density profile for DM subhalos [25-27].

$$\rho(r) = \frac{\rho_0}{(r/\text{kpc})^\gamma} e^{-r/R_b}. \quad (\text{S-8})$$

The parameters ρ_0 , γ and R_b can be parametrized as $\gamma(d) = g_1(d/\text{kpc})^{g_2}$ and $R_b = b_1(d/\text{kpc})^{b_2}$, where $d \approx 8.5$ kpc is the distance from the center of the subhalo to the GC. The values of the parameters $g_{1,2}$ and $b_{1,2}$ can be extrapolated from the N-body simulations for different ranges of the total mass M_h . For fixed r and R_b , the normalization factor ρ_0 can be determined by the subhalo total mass M_h . Based on a joint analysis to the Via Lactea II and ELVIS simulations in Ref. [27], we obtain the values of γ , R_b and ρ_0 for selected values of M_h , which are listed in Tab. S-3.

$M_h (M_\odot)$	γ	R_b (kpc)	ρ_0
1×10^6	0.81	0.054	1.8
1×10^7	0.78	0.096	5.3
3×10^7	0.65	0.19	4.5
1×10^8	0.75	0.22	9.4

TAB. S-3: Parameters of DM subhalo density profiles extrapolated to the distance $d \approx 8.5$ kpc for different choices of the subhalo masses from [27]. The reference density ρ_0 is in units of $\text{GeV} \cdot \text{cm}^{-3}$.

For a typical subhalo masses $M_h = 10^7 M_\odot$, the best-fit parameters for three choices of (r, m_χ) are shown in Tab. S-4, which correspond to the three cases plotted in the middle panel of Fig. 2. Similar to the case of continuous point-like sources, when r is allowed to vary freely, the value of χ^2 decreases with decreasing distance and approaches a minimal value $\chi_{\min}^2 = 13.2$ in the limit of $r \rightarrow 0$. The allowed regions at 68% (95%) C.L. in (r, m_χ) and $(r, \langle\sigma v\rangle)$ planes are shown in Fig. S-3. The allowed range of distance is $r \lesssim 0.3$ kpc at 95% C.L., which is almost the same as that in the case of mini-spikes. The fit results for other subhalo masses $M_h = 10^6 M_\odot$, $3 \times 10^7 M_\odot$ and $10^8 M_\odot$ are shown separately in Tab. S-5. The results show that the DAMPE excess can be well fitted for a large range of M_h . Increasing the value of M_h leads to a decrease of the DM annihilation cross section.

r [kpc]	m_χ [GeV]	$\langle\sigma v\rangle$	γ_1	γ_2	N_b	$\chi^2/\text{d.o.f.}$
0.1	1510	1.04 ± 0.30	3.10 ± 0.01	$4.08_{-0.13}^{+0.14}$	1.90 ± 0.03	13.37/28
0.2	1520	$2.55_{-0.83}^{+0.82}$	3.10 ± 0.01	$4.10_{-0.13}^{+0.15}$	1.90 ± 0.03	15.90/28
0.3	1550	$4.62_{-1.87}^{+1.83}$	3.10 ± 0.01	$4.10_{-0.14}^{+0.16}$	1.89 ± 0.03	19.20/28

TAB. S-4: Best-fit parameters for three choices of (r, m_χ) values for a source of DM subhalo with mass $M_h = 10^7 M_\odot$. The corresponding subhalo density parameters are listed in Tab. S-3. $\langle\sigma v\rangle$ is in units of $10^{-26} \text{cm}^3 \text{s}^{-1}$ and N_b is in units of $10^{-7} \text{GeV}^{-1} \text{m}^{-2} \text{s}^{-1} \text{sr}^{-1}$.

$M [M_\odot]$	r [kpc]	m_χ [GeV]	$\langle\sigma v\rangle$	γ_1	γ_2	N_b	$\chi^2/\text{d.o.f.}$
10^6	0.1	1510	15.15 ± 4.32	3.10 ± 0.01	$4.08_{-0.13}^{+0.14}$	1.90 ± 0.03	13.26/28
–	0.2	1520	$39.88_{-12.83}^{+12.79}$	3.10 ± 0.01	$4.10_{-0.13}^{+0.15}$	1.90 ± 0.03	15.81/28
–	0.3	1550	$72.9_{-29.29}^{+28.73}$	3.10 ± 0.01	$4.10_{-0.13}^{+0.16}$	1.89 ± 0.03	19.15/28
3×10^7	0.1	1510	1.49 ± 0.44	3.10 ± 0.01	$4.08_{-0.13}^{+0.14}$	1.90 ± 0.03	13.88/28
–	0.2	1520	$2.95_{-0.94}^{+0.93}$	3.10 ± 0.01	$4.11_{-0.14}^{+0.15}$	1.90 ± 0.03	16.43/28
–	0.3	1550	$4.93_{-2.05}^{+2.03}$	3.10 ± 0.01	$4.11_{-0.14}^{+0.16}$	$1.89_{-0.04}^{+0.03}$	19.60/28
10^8	0.1	1510	0.17 ± 0.05	3.10 ± 0.01	$4.08_{-0.13}^{+0.14}$	1.90 ± 0.03	13.89/28
–	0.2	1520	0.33 ± 0.11	3.10 ± 0.01	$4.11_{-0.14}^{+0.15}$	1.90 ± 0.03	16.46/28
–	0.3	1550	$0.55_{-0.23}^{+0.22}$	3.10 ± 0.01	$4.11_{-0.14}^{+0.16}$	$1.89_{-0.04}^{+0.03}$	19.64/28

TAB. S-5: The same as Tab. S-4, but with different DM subhalo masses $M_h = 10^6 M_\odot$, $3 \times 10^7 M_\odot$ and $10^8 M_\odot$. The corresponding DM subhalo density parameters are listed in Tab. S-3.

Contributions from the Galactic halo DM

For DM sources, the contributions to CRE also come from the whole Galactic DM halo. If the favoured DM annihilation cross sections are around the thermal value $\langle\sigma v\rangle_F = 3 \times 10^{-26} \text{cm}^3 \text{s}^{-1}$, the contributions to the CRE flux from the whole Galactic DM above TeV are found to be negligibly small. In Fig. S-4, we compare the contributions to CRE from DM substructures and DM Galactic halo for typical cases. For calculating the contributions from Galactic DM halo, we make use of the GALPROP v54 package [32] with a reference propagation parameter set $SLZ6R20T100000C5$ [33] and the Einasto DM profile with a local DM density of 0.4GeVcm^{-3} . The contributions from remote DM subhalos in the Galaxy can be safely neglected, as the N-body simulations show that they contribute only to a tiny fraction of the total Galactic DM mass [22-24].

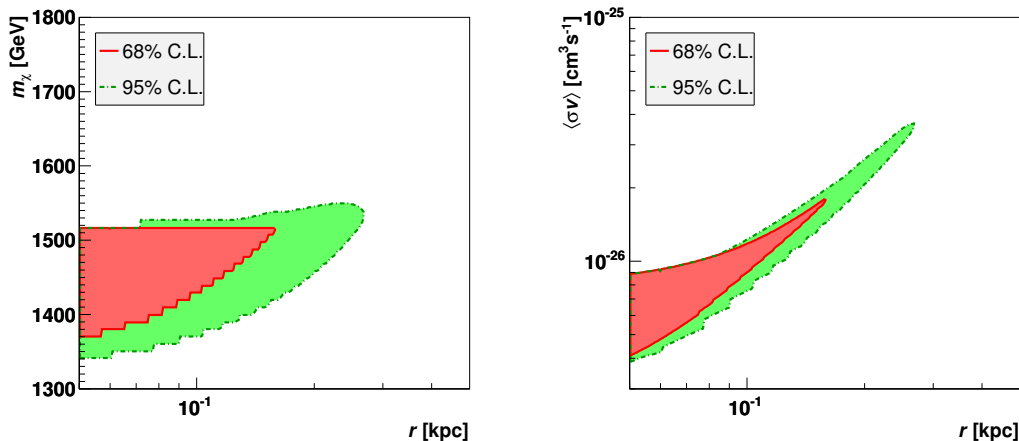


FIG. S-3: Left) Allowed regions at 68% and 95% C.Ls. in (r, m_χ) plane for the source of DM subhalos. Right) Allowed region in $(r, \langle\sigma v\rangle)$ plane.

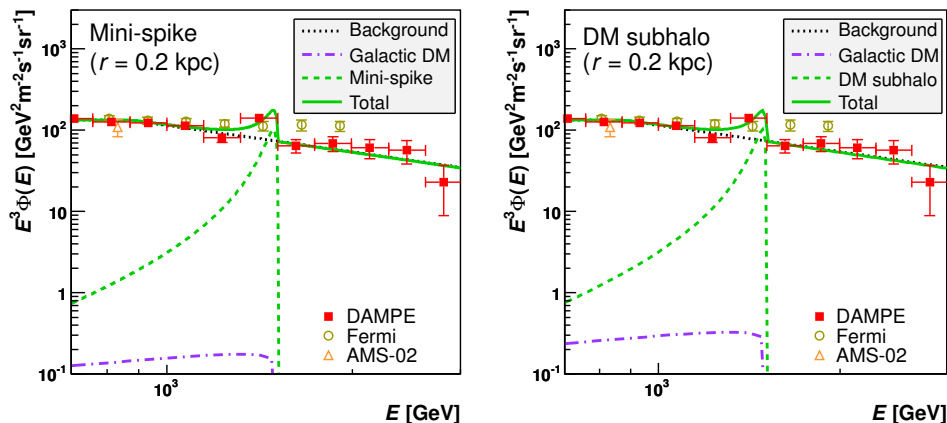


FIG. S-4: Left) Comparison of the CRE energy spectrum from a mini-spike and that from the whole Galactic halo DM with the same DM annihilation cross section. The parameters of the mini-spike correspond to the case of $r = 0.2$ kpc in Tab. S-2. Right) Comparison of electron energy spectrum from a nearby DM subhalos and that from the whole Galactic halo DM with the same annihilation cross section. The parameters of the DM subhalo correspond to the case of $r = 0.2$ kpc in Tab. S-4.

C. Burst-like sources

For the burst-like sources, the best-fit parameters for three representative choices of (r, α) shown in the right panel of Fig. 2 in the letter are summarized in Tab. S-6, where the total released energy E_{tot} is derived from the value of N_0 , using $E_{\text{tot}} = \int_{E_{\text{min}}} EQ(r, t, E) dE d^3r dt$ with a lower cutoff $E_{\text{min}} = 0.1$ GeV. When r and α are allowed to vary freely in the fit, the χ^2 gradually approaches a minimal value of 12.5 for $\alpha \rightarrow 0$. The allowed regions in (r, α) at 68% and 95% C.L. are shown in Fig. S-5. In the region $r \leq r_d(E_{\text{max}})$, the favoured α is less than 0.65 at 95% C.L. which is highly insensitive to the distance, as the spectral shape is dominated by the effect of “phase-space shrinking”. In the region $r > r_d(E_{\text{max}})$, the effect of energy-dependent diffusion becomes important and the allowed value of α can be larger which can reach 1.3 (1.6) at $r \approx 3(4)$ kpc. By imposing the condition of $E_{\text{tot}} < 10^{51}(10^{53})$ erg, the distance r is restricted in range $r \lesssim 3(4)$ kpc. Together with the required $t = (1.5 - 1.7) \times 10^5$ yr, we find the 7 candidate pulsars in the ATNF catalogue. The relevant parameters of these candidates are summarized in Tab. S-7.

r [kpc]	α	t (Myr)	N_0 (GeV $^{-1}$)	γ_1	γ_2	N_b	$\chi^2/\text{d.o.f.}$
1.0	0.5	$0.147^{+0.002}_{-0.003}$	$3.72^{+1.18}_{-1.21} \times 10^{44}$	3.10 ± 0.01	$4.09^{+0.15}_{-0.13}$	1.90 ± 0.03	15.56/27
2.0	0.7	$0.147^{+0.002}_{-0.003}$	$2.33^{+0.74}_{-0.79} \times 10^{46}$	3.10 ± 0.01	$4.09^{+0.15}_{-0.13}$	1.90 ± 0.03	15.62/27
3.0	1.3	$0.146^{+0.002}_{-0.003}$	$3.10^{+1.13}_{-1.26} \times 10^{50}$	3.10 ± 0.01	$4.10^{+0.16}_{-0.14}$	1.90 ± 0.03	17.51/27

TAB. S-6: Best-fit parameters for three representative choices of (r, α) in the case of burst-like sources. The cutoff energy is fixed at $E_c = 5 \times 10^4$ GeV. N_b is in units of $10^{-7} \text{GeV}^{-1} \text{m}^{-2} \text{s}^{-1} \text{sr}^{-1}$. The total released energy for the cases of $r = 1, 2$ and 3 kpc is $E_{\text{tot}} = 2.53^{+0.80}_{-0.82} \times 10^{48}$, $2.18^{+0.70}_{-0.74} \times 10^{49}$ and $9.56^{+3.49}_{-3.88} \times 10^{50}$ erg, respectively.

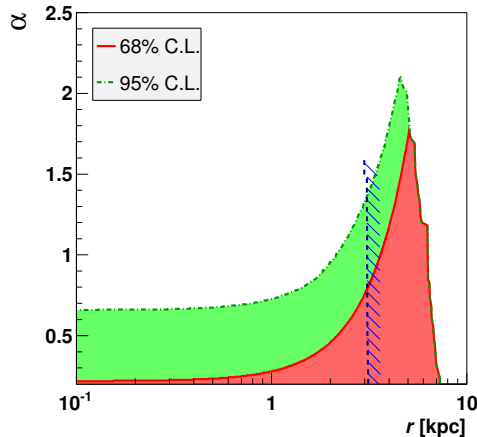


FIG. S-5: Allowed regions at 68% and 95% C.L. in (r, α) plane for the burst-like point source. The region excluded at large distances $r \gtrsim 3$ kpc is due to the requirement that the total energy $E_{\text{tot}} < 10^{51}$ erg.

D. Electron anisotropies

For one or a few nearby sources, the anisotropy in the arrival directions of CREs is dominated by the dipole term which can be approximated as

$$\Delta \approx \frac{3D(E)}{c} \left| \frac{\nabla \Phi_{\text{tot}}}{\Phi_{\text{tot}}} \right|, \quad (\text{S-9})$$

where Φ_{tot} is the total flux of the nearby sources and the background, and c is the speed of light. In the approximation that the background is nearly isotropic, the anisotropy for the continuous point-like sources is given by

$$\Delta_{\text{conti}} \approx \frac{3r}{2c} \frac{(1-\delta)b_0 E}{[1 - (E/E_0)^{1-\delta}]} \frac{f(r, E)}{f_{\text{tot}}(r, E)}, \quad (\text{S-10})$$

Source Name	ℓ (deg)	b (deg)	r (kpc)	t (yr)	\dot{E} (erg/s)
B0740-28	243.77	-2.44	2.00	1.57×10^5	1.4×10^{35}
J0922-4949	272.24	0.16	2.70	1.54×10^5	4.5×10^{33}
J1055-6022	289.11	-0.65	3.60	1.62×10^5	4.3×10^{33}
J1151-6108	295.81	0.91	2.22	1.57×10^5	3.9×10^{35}
J1509-5850	319.97	-0.62	3.35	1.54×10^5	5.1×10^{35}
J1616-5017	332.83	0.29	3.48	1.67×10^5	1.6×10^{34}
J1739-3023	358.09	0.34	3.07	1.59×10^5	3.0×10^{35}

TAB. S-7: Parameters of candidate pulsars in ATNF pulsar catalog [30] satisfying the conditions of age $t = 0.15 - 0.17$ Myr as required to reproduce the DAMPE excess, and distance $r < 4$ kpc from the requirement of $E_{\text{tot}} < 10^{53}$ erg. The quantities (ℓ, b) , r , t and \dot{E} stand for the direction, distance, age and spin-down energy loss rate, respectively.

where $f_{\text{tot}} = f(r, E) + f_{\text{bg}}(r, E)$ is the total distribution function. For the burst-like source it can be written as

$$\Delta_{\text{burst}} \approx \frac{3r}{2ct} \frac{(1-\delta)E/E_{\text{max}}}{1-\xi(E)^{1-\delta}} \frac{f(r, E)}{f_{\text{tot}}(r, E)}. \quad (\text{S-11})$$

The predicted anisotropies according to the best-fit parameters in each case of the three type of sources listed in Tab. S-2, Tab. S-4 and Tab. S-6 are shown in Fig. S-6. The anisotropy of the background CRE depends on the assumed spatial distribution of primary CRE sources, the typical values estimated from GALPROP is of $\mathcal{O}(10^{-3})$ [31] which is significantly smaller than that generated from nearby sources.

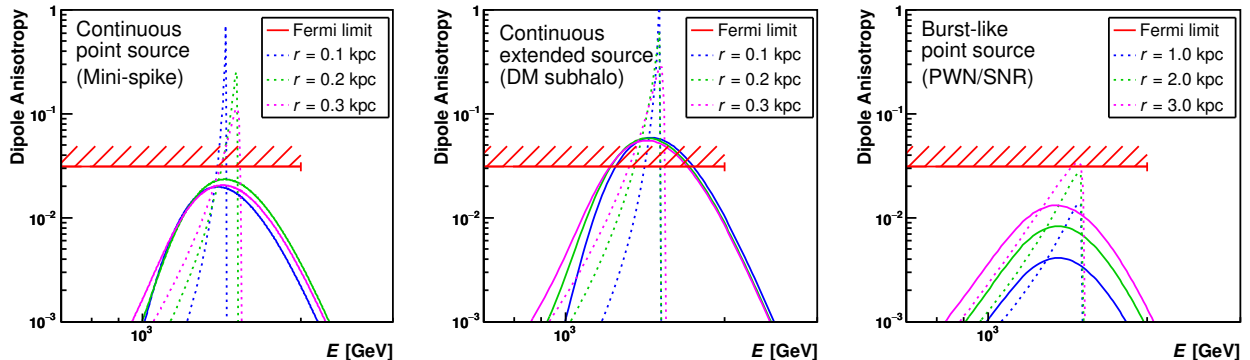


FIG. S-6: Predictions for electron anisotropies in the arrival directions (dotted curves). Left) for continuous point-like sources with three parameter sets listed in Tab. S-2 Middle) for continuous extended sources with parameter sets listed in Tab. S-4. Right) for burst-like sources with parameter sets listed in Tab. S-6. For all the type of sources, the dashed curves correspond to the anisotropies convoluted with an energy resolution of 15%, and the horizontal lines indicate the averaged value in the energy bin 0.55-2 TeV, the corresponding current upper limits from Fermi-LAT are also shown.

E. Associated gamma-ray signals

Prompt gamma-rays

Prompt photons are generated from DM annihilation through FSR of final state charged leptons, which is of particular importance for electron final states. The flux of FSR photon from the annihilation of Majorana DM particles (with mass m_χ) per solid angle $d\Omega$ is given by

$$\frac{d\Phi_\gamma}{d\Omega dE_\gamma} = \frac{\langle\sigma v\rangle}{8\pi m_\chi^2} \frac{dN_\gamma}{dE_\gamma} \int_{\text{l.o.s}} \rho^2(r') ds. \quad (\text{S-12})$$

where $\rho(r')$ is the DM density profile, and the integration is performed along the light-of-sight s which is related to r' as $r' = \sqrt{s^2 + r^2 - 2sr \cos\theta}$ with r the distance from the detector to the center of the DM halo and θ is the angle away from the center. The spectrum for e^+e^- final state is given by

$$\frac{dN_\gamma}{dx} = \frac{\alpha_{\text{em}}}{\pi} \frac{1 + (1-x)^2}{x} \left[-1 + \ln\left(\frac{4(1-x)}{\epsilon^2}\right) \right], \quad (\text{S-13})$$

where $x = E_\gamma/m_\chi$, $\epsilon = m_e/m_\chi$ and α_{em} is the fine structure constant. An important feature of the FSR photon spectrum is that it can be approximated as a power law at low energies

$$\frac{dN_\gamma}{dE} \propto E^{-1}, \quad (\text{for } E_\gamma \ll m_\chi) \quad (\text{S-14})$$

and has a sharp cutoff at $E_\gamma = m_\chi$. In numerical calculations we use the package PYTHIA 8.1 which adopts the same formula. Since mini-spikes are point-like, the flux of prompt γ -rays from DM annihilation in mini-spikes can be approximated as

$$\frac{d\Phi_\gamma}{dE_\gamma} = \frac{\langle\sigma v\rangle}{2m_\chi^2} \frac{L}{4\pi r^2} \frac{dN_\gamma}{dE_\gamma}, \quad (\text{S-15})$$

where L is the annihilation luminosity given in the letter, and r is the distance from the detector to the center of the mini-spike. The prompt γ -rays from DM subhalos and Galactic DM are calculated by direct integration over the DM density profile. Unlike the case of the CRE, for prompt γ -rays, the contribution from the whole Galactic halo DM is significant.

ICS gamma-rays

The distribution of final state photon from the ICS process $e(E_e) + \gamma(E_\gamma) \rightarrow e'(E'_e) + \gamma'(E'_\gamma)$, where $E_e(E'_e)$, $E_\gamma(E'_\gamma)$ are the energies of initial (final) state electron and photon, respectively, is given by

$$\frac{dN_{\gamma'}}{dE_{\gamma'} dt} = 2\pi\alpha_{\text{em}}^2 \frac{u_\gamma}{E_e^2 E_\gamma^2} f_{\text{IC}}(q, \varepsilon), \quad (\text{S-16})$$

where u_γ is the energy density of the initial photons. The function $f_{\text{IC}}(q, \varepsilon)$ is

$$f_{\text{IC}}(q, \varepsilon) = 2q \ln(q) + (1 + 2q)(1 - q) + \frac{(\varepsilon q)^2}{2(1 + \varepsilon q)}(1 - q), \quad (\text{S-17})$$

where $\varepsilon = E'_\gamma/E_e$, $\Gamma = 4E_\gamma E_e/m_e^2$ and $q = \varepsilon/\Gamma(1 - \varepsilon)$. The final energy satisfies the relation $E'_\gamma/E_e \leq \varepsilon \leq \Gamma/(1 + \Gamma)$. The photon flux $\Phi_\gamma = dN_\gamma/dAdt$ obtained for a given line of sight is [42]

$$\frac{d^2\Phi_{\gamma'}}{dE_{\gamma'} d\Omega} = \frac{1}{2}\alpha_{\text{em}}^2 \int_{\text{l.o.s.}} ds \int \int \frac{dE_e}{E_e^2} \frac{dE_\gamma}{E_\gamma^2} f(r, E_e) u_\gamma(E_\gamma) f_{\text{IC}}, \quad (\text{S-18})$$

where $f(r, E_e)$ is the density of initial state electrons. The energy density $u_\gamma(E_\gamma)$ is assumed to be black body like

$$u_\gamma(E_\gamma) = \mathcal{N} \frac{E_\gamma^3}{\pi^2 (e^{E_\gamma/T} - 1)}, \quad (\text{S-19})$$

where \mathcal{N} is a position-dependent normalization constant. The three major components of the ISRF are cosmic microwave background with temperature $T_{\text{CMB}} = 2.35 \times 10^{-4}$ eV, the infrared radiation produced by the absorption and re-emission of star light by the interstellar dust with temperature $T_{\text{dust}} = 3.5 \times 10^{-3}$ eV and the star light with temperature $T_{\text{star}} = 0.3$ eV. For the normalization factors, we use the values $\mathcal{N}_{\text{CMB}} = 1$, $\mathcal{N}_{\text{dust}} = 2.5 \times 10^{-5}$ and $\mathcal{N}_{\text{star}} = 6.0 \times 10^{-13}$, respectively, which are the values at the solar neighbourhood $d \approx 8$ kpc interpolated from [34].

Gamma-ray signals of mini-spikes, DM subhalos and burst-like sources

In the top-left panel of Fig. S-7, we show the spatial extension of the γ -ray flux (with energy above 1 GeV) of the mini-spike with the parameters corresponding to the best-fit values in the case of $r = 0.2$ kpc in Tab. S-2 and the direction of the location coincides with the GC. The corresponding DM annihilation cross section is $\langle\sigma v\rangle = 1.36 \times 10^{-26}$ cm³s⁻¹ according to Eq. (3) in the letter. In the figure, the contributions of prompt and ICS photons are shown explicitly. For mini-spikes, the spatial extension is $\ll 1^\circ$ within 68% containment. Thus they can be treated as point-like sources. For the three cases considered in Tab. S-2, the total fluxes integrated in the energy range 1 – 100 GeV are in the range $(0.47 - 1.01) \times 10^{-10}$ cm⁻²s⁻¹, which are within the current sensitivity of Fermi-LAT in point-source searches. For the point-source searches, the energy spectrum is dominated by the FSR photons. Thus the expected spectrum should have a power index close to ~ 1 . In the Fermi-LAT 3FGL catalog of unassociated point sources (sources that have not been associated with emission observed at other wavelengths), we find 6 candidate sources with low power indexes (index α can reach 1.0 within 2σ error), which are listed in the Tab. S-8. It is also possible that the mini-spike is located in the direction of the low Galactic latitudes where the Fermi-LAT sensitivity is much lower.

Source Name	ℓ (deg)	b (deg)	Φ ($10^{-10} \text{cm}^{-2} \text{s}^{-1}$)	α	Significance (σ)
J0603.3+2042	189.124	-0.690422	6.180	1.50 ± 0.50	4.37156
J1250.2-0233	302.344	60.3066	0.926 ± 0.521	1.10 ± 0.30	5.12018
J2209.8-0450	55.6854	-45.5583	1.784 ± 0.974	1.27 ± 0.32	6.46061
J1705.5-4128c	345.052	-0.281031	48.379	2.77 ± 1.06	5.12339
J2142.6-2029	31.1422	-46.5567	1.245 ± 0.683	1.52 ± 0.33	4.05409
J2300.0+4053	101.243	-17.2428	1.719 ± 0.746	1.51 ± 0.26	5.2434

TAB. S-8: Parameters of selected point sources in the Fermi-LAT 3FGL “unassociated” point-source catalog [35], which have power-law type of spectrum with low power indices (the power index α can reach one with 2σ error) and are possibly due to FSR of DM particles in mini-spikes. The total flux is integrated from 1 to 100 GeV.

In the top-right panel of Fig. S-7, we show the spatial extension of the DM subhalo with the parameters corresponding to the best-fit values in the case of $r = 0.2$ kpc of Tab. S-4, and the direction of the location coincides with the GC. It can be seen that the γ -rays are significantly extended to a few tens of degrees, as they are dominated by the ICS photons. In Fig. S-7, for a comparison, we also show the prompt and ICS photons from the Galactic halo DM with the same DM annihilation cross section, which is calculated by using GALPROP with the same parameter set as that use in obtaining the Fig. S-4. Unlike the case of electrons, the contribution to diffuse γ -ray from the Galactic halo DM is very significant.

The γ -ray energy spectra of mini-spikes and DM subhalos are shown in the left and right panels of Fig. S-7, respectively. The spectra are averaged over two regions of interest (ROI) which represent the low and high Galactic latitude limits, one is a circular ROI with an angular radius 30° centered at the GC ($\ell = 0^\circ$ and $b = 0^\circ$), the other one has the same shape but centered at high latitude ($\ell = 0^\circ$ and $b = 90^\circ$). The components of prompt and ICS photons are explicitly shown. The contributions from the Galactic halo DM are included in the same way. At low latitudes close to the Galactic disk the contributions of ICS photons are significant, which is expected as the ISRF has large intensity. After summing up all the components of the contributions, the total spectrum scales with energy approximately as E^{-2} with a sharp cutoff at the DM particle mass m_χ . On the other hand, at high latitudes, the FSR photons are dominant at high energies, and the spectrum scales approximately as E^{-1} .

The spatial extension and energy spectra of γ -rays in all the cases of the three type of sources listed in Tabs. S-2, S-4 and S-6 are summarized in Fig. S-8, together with the calculated Galactic diffuse γ -ray backgrounds in the same ROIs. The figure shows that at high latitude $b = 90^\circ$, the predicted flux of burst-like source can exceed the diffuse background. Since the background is in an overall agreement with the Fermi-LAT data, this scenario is disfavoured. We thus conclude that the sources are more likely to be located at relatively low Galactic latitudes where the background is large.

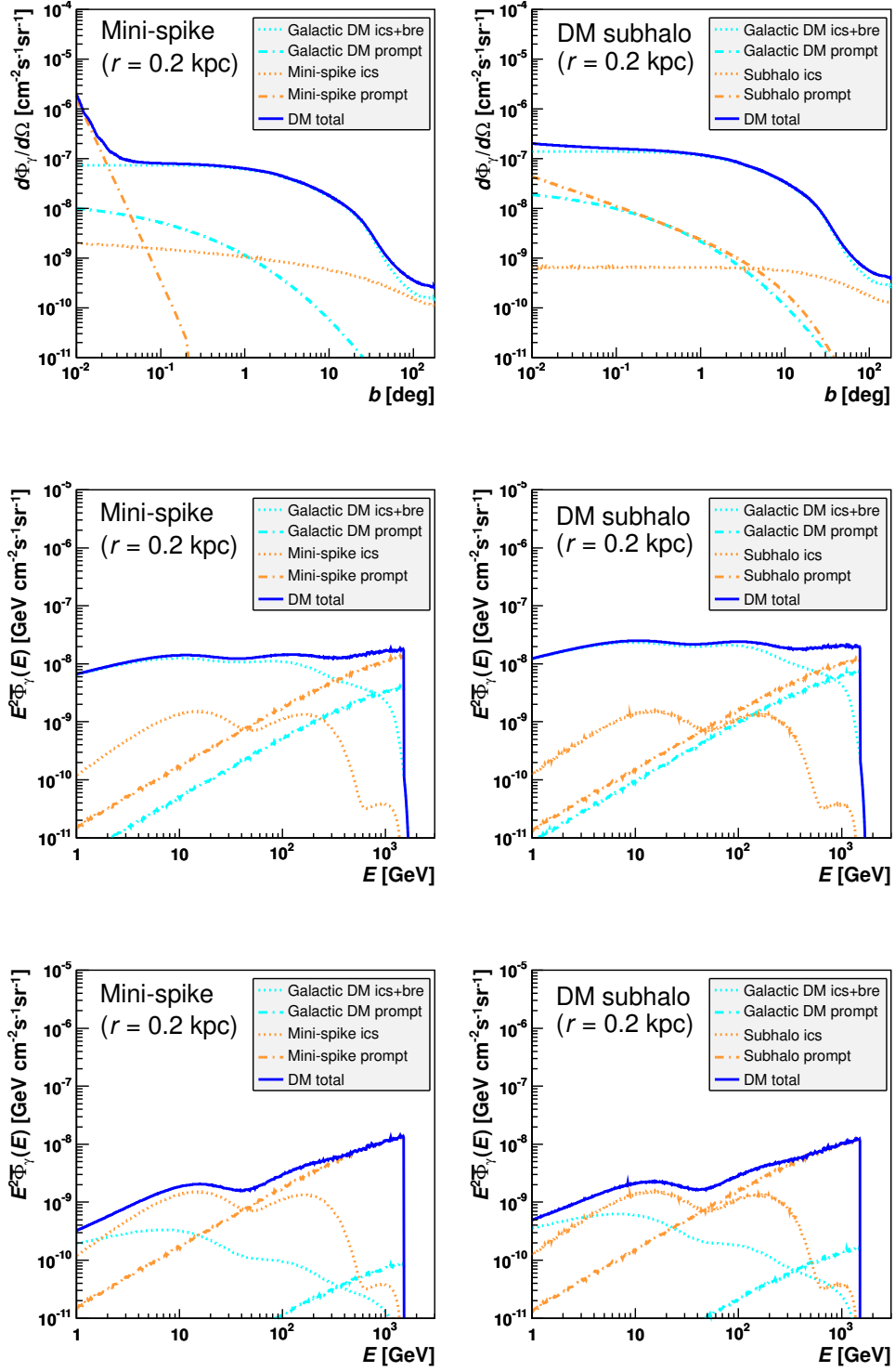


FIG. S-7: Left panels) Top: spatial extension of the γ -ray flux (above 1 GeV) of the mini-spike with parameters corresponding to the case of $r = 0.2$ kpc in Tab. S-2. The contributions from prompt and ICS photons are shown explicitly, together with that from the Galactic halo DM. Middle: averaged energy spectrum of γ -rays over the ROI of a circular region with angular radius 30° centered at GC ($\ell = 0^\circ, b = 0^\circ$) for the same parameters. Bottom: the same as middle panels but for the ROI centered at ($\ell = 0^\circ$ and $b = 90^\circ$). Right panels) The same as left, but for the DM subhalos with parameters corresponding to the case of $r = 0.2$ kpc in Tab. S-4.

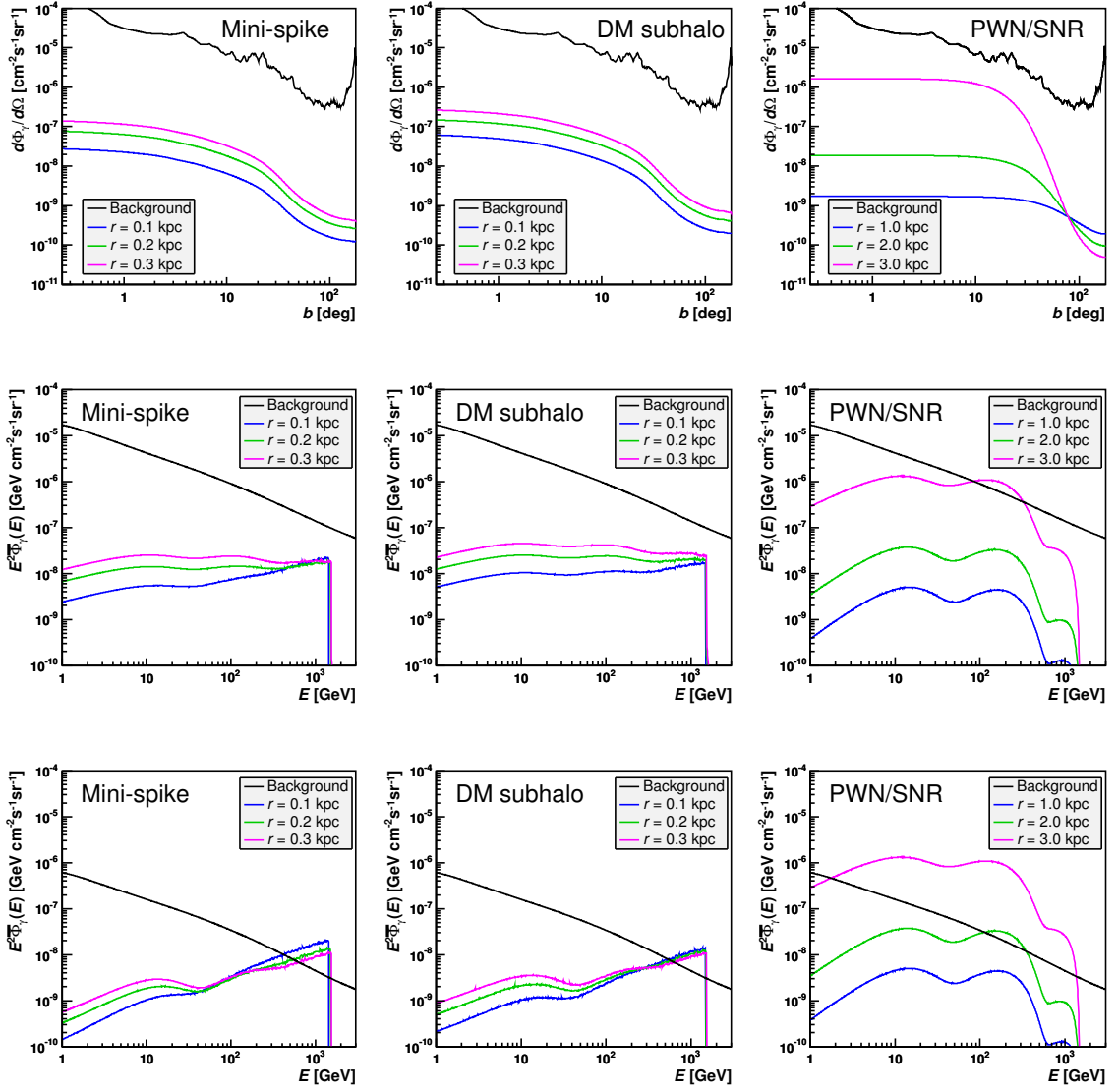


FIG. S-8: Predicted γ -ray spatial extension and energy spectra for all the three parameter sets in the three type of sources considered in Fig. 2 in the letter with all the components summed up together. Left panels) for mini-spikes with parameters in Tab. S-2 Center panels) for DM subhalos with parameters in Tab. S-4 Right panels) for burst-like sources with parameters in Tab. S-6. The ROI are the same as that in Fig. S-7. The corresponding Galactic diffuse γ -ray backgrounds are also shown.